

RESEARCH ARTICLE

10.1002/2014JB011560

Key Points:

- Seismograms recorded on Greendale Fault show persistent wavefield polarization
- Ambient noise is affected by unconsolidated sediments over the bedrock
- Polarization is interpreted as the effect of larger crack-transverse compliance

Supporting Information:

- Figures S1 and S2

Correspondence to:

M. Pischietta,
marta.pischietta@ingv.it

Citation:

Pischietta, M., M. K. Savage, R. A. Holt, and F. Salvini (2015), Fracture-related wavefield polarization and seismic anisotropy across the Greendale Fault, *J. Geophys. Res. Solid Earth*, 120, 7048–7067, doi:10.1002/2014JB011560.

Received 22 AUG 2014

Accepted 22 SEP 2015

Accepted article online 29 SEP 2015

Published online 21 OCT 2015

Fracture-related wavefield polarization and seismic anisotropy across the Greendale Fault

M. Pischietta¹, M. K. Savage², R. A. Holt², and F. Salvini³
¹Istituto Nazionale di Geofisica e Vulcanologia, Roma, Italy, ²Institute of Geophysics, Victoria University of Wellington, Wellington, New Zealand, ³Earth Science Department, RomaTre University, Rome, Italy

Abstract We investigate seismic signatures of fracturing in a newly ruptured strike-slip fault by determining the wavefield polarization in the New Zealand Canterbury Plains area and across the Greendale Fault, which was responsible for the 3 September 2010 Darfield Mw 7.1 earthquake. Previous studies suggested that fractured rocks in fault damage zones cause directional amplification and ground motion polarization in the fracture-perpendicular direction as an effect of stiffness anisotropy, and cause velocity anisotropy with shear wave velocity larger in the fracture-parallel component. An array of 14 stations was installed following the Darfield earthquake. We assess polarization both in the frequency and time domains through the individual-station horizontal-to-vertical spectral ratio and covariance matrix analysis, respectively, and compare the results to previously reported anisotropy measurements from shear wave splitting. Stations installed in the Canterbury Plains have an amplification peak between 0.1 and 0.3 Hz for both earthquakes and ambient noise. We relate the amplification to the resonance of a considerable thickness (c. 1 km) of soft sediments lying over the metamorphic bedrock. Analysis of seismic events revealed the existence of another peak in amplification between 2 and 5 Hz at two on-fault stations, which was not visible in the noise analysis. In contrast to the lower frequency peak, the ones between 2 and 5 Hz are more strongly anisotropic, attaining amplitudes up to a factor of 4 in the N52° direction. To interpret this effect we model the fracture pattern in the fault damage zone produced by the fault kinematics. We conclude that the horizontal polarization is orthogonal to extensional fractures, which predominate in the shallow layers (<2 km) with an expected strike of N139°. Fracture orientation is consistent with coseismic surface rupture observations, confirming the reliability of the model. *S* wave splitting is produced by velocity anisotropy in the entire rock volume crossed along the seismic path; thus, it is affected by deeper material than the amplification study. We explain the rotation of *S* wave fast component observed by Holt et al. (2013) near the fault in terms of the dominant synthetic cleavages at greater depths (>2 km), expected in N101° direction on the basis of the model. Thus, different fracture distribution at different depths may explain different results for amplification compared to anisotropy. We propose polarization amplification analysis as a complementary method to *S* wave splitting analysis. Polarization analysis is rapidly computed and robust, and it can be applied to either earthquakes or ambient noise recordings, giving useful information about the predominant fracture patterns at various depths.

1. Introduction

Fault zone structures and fabric may control the mode of propagation or the likelihood of breakage; therefore, studying them may help to understand how earthquakes occur and thus also determine seismic hazards. Yet many, if not most, faults are buried and seismic methods are one of the few ways to probe them. Differential amplifications of the horizontal ground motions can also cause unusual damage to buildings and structures. Thus, the analysis of polarization and resonance effects can provide information on key properties of the subsurface structure and expected shaking hazard [Bard, 1998; Panzera et al., 2014]. Yet polarization studies have not been widely applied or compared to newly broken faults. Here we compare two methods of measuring seismic wavefield polarization in a newly ruptured surface fault and relate them to fractures and sheared fabric within the fault zone.

In the crust, seismic anisotropy is mostly caused by the orientation of microcracks aligned by the stress field [e.g., Nur and Simmons, 1969; Crampin, 1994]. However, in fault zones, *S* wave fast directions, as measured by shear wave splitting, are often controlled by the shear fabric of the fault damage zone [e.g., do Nascimento et al., 2002; Peng and Ben-Zion, 2004; Balfour et al., 2005; Cochran et al., 2006]. Recently, directional

amplification of horizontal ground motion has also been observed in fault zones [e.g., *Falsaperla et al.*, 2010; *Pischiutta et al.*, 2012; *Di Giulio et al.*, 2009, 2013] and has been associated with densely fractured rocks, the predominant direction tending to be oriented perpendicularly to the predominant fracture field [e.g., *Pischiutta et al.*, 2012, 2013].

Several authors studied seismic anisotropy in the San Andreas fault zone, finding near fault-parallel *S* wave fast directions as well as high time delays, indicative of high anisotropy [Zhang and Schwartz, 1994; Liu et al., 1997; Zinke and Zoback, 2000; Cochran et al., 2003; Paulssen, 2004; Boness and Zoback, 2004, 2006]. Cochran et al. [2006] ascribed these observations to densely fractured rocks in the fault zone.

Pischiutta et al. [2014] recently studied ground motion polarization in the Valdagri region, Italy, an area well exploited by hydrocarbon exploration. They found an orthogonal relation between ground motion polarization and *S* wave fast direction that was interpreted as the effect of fracture orientations on both the velocity anisotropy of seismic waves (they travel faster when the direction of propagation is parallel to fractures) and on azimuthally dependent amplification, which leads to horizontal polarization (fractured rocks are more compliant in the direction orthogonal to the fractures).

To see whether such effects are observable in a newly fractured strike-slip fault system, in this paper we study ground motion polarization in the Greendale Fault area, New Zealand, and compare results to the shear wave splitting by *Holt et al.* [2013]. The orthogonal relation between polarization and anisotropy is confirmed at one station located in the fault damage zone. Following the approach by *Pischiutta et al.* [2013], we also model the predicted fracture field by using the package FRAP [Salvini et al., 1999] and interpret ground motion polarization in terms of fractures and seismic anisotropy in the fault damage zone.

2. The Study Area

The right-lateral strike-slip Greendale Fault is located near the dextral-transpressional deformation zone associated with the oblique collision of the Pacific plate with the Australian plate in New Zealand. This fault was unknown before the 2010–2011 Canterbury earthquake sequence, which started on 3 September 2010 with the Darfield Mw 7.1 earthquake. GPS and InSAR data suggest that the rupture process involved the failure of multiple fault segments [Beavan et al., 2011; Gledhill et al., 2011]. The rupture propagated upward from the nucleation point at 6 km depth and to the south along strike [Holden, 2011], finally forming a rupture surface extending east-west for ~30 km [Quigley et al., 2010]. Field evidence, aftershock locations, and focal mechanisms confirm a dextral displacement consistent with pure strike-slip kinematics on a subvertical surface [e.g., Beavan et al., 2011; Gledhill et al., 2011]. The displacement was observed symmetrically along the fault in a ~30 to 300 m wide zone, with an average horizontal slip of 2.5 m. The morphological signature of the rupture is represented by an en echelon series of E-W trending left-stepping surface traces [Van Dissen et al., 2011] up to 1 km wide. The distribution of aftershocks [Gledhill et al., 2011; Syracuse et al., 2013] indicates a complex fault system that *Sibson et al.* [2011] described as “immature” considering (i) the presence of conjugate fault sets and (ii) the coexistence of reactivated inherited basement faults and low-displacement faults formed within the contemporary stress field. Moreover, the major E-W dextral trend is crosscut by left-lateral strike-slip conjugate faults that create contractional jogs acting as high-strength asperities [Sibson et al., 2011]. Modeling of fault zone trapped waves suggested that damage extends to a depth of 8 km or deeper, with a velocity reduction of 35–55% in a zone of 200–250 m wide; the most highly damaged core is 100 m wide [Li et al., 2014]. *Holt et al.* [2013] determined focal mechanisms and shear wave splitting from about 2000 earthquakes in the area, determining an average maximum horizontal stress direction of $116 \pm 18^\circ$. They also found that in the upper 8 km of the crust, the stress field along the fault was rotated to being more fault parallel, i.e., closer to E-W, and suggested that the rotation was caused by a high stress drop of 40% during the earthquake, or else that the stress field was constant but severely misoriented for rupture before the earthquake.

On 22 February 2011, a Mw 6.2 earthquake occurred beneath the city of Christchurch [Kaiser et al., 2012]. It was generated by an oblique thrust fault located near the Banks peninsula [Ghisetti and Sibson, 2012]. In contrast to the Darfield earthquake, which occurred in a sparsely populated area, the Christchurch earthquake caused severe damage throughout the city, causing loss of life and property. Serious damage due to extensive soil liquefaction was associated with both these earthquakes [Cubrinovsky et al., 2011; Orense et al., 2011]. No field evidence was found for the Christchurch earthquake causative fault due to the

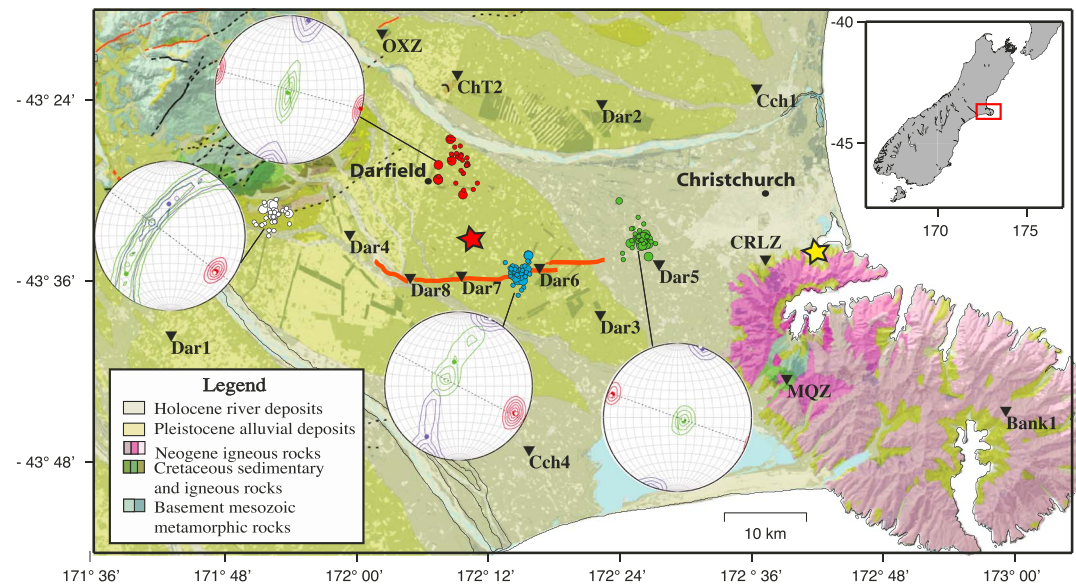


Figure 1. Geologic map of the Canterbury Plains [modified after Forsyth *et al.*, 2008]. Black reverse triangles indicate the location of seismic stations used in this study. The red star represents the epicenter of the M 7.1 Darfield 3 September 2010 earthquake. The yellow star represents the epicenter of the M 6.3 Christchurch 22 February 2011 earthquake. The red line is the morphological signature of the rupture that was produced by the main shock [Van Dissen *et al.*, 2011]. We indicate the earthquake epicenters of seismic events used in this study through circles whose dimension is related to the hypocentral depth (green = CI-2; red = CI-4; blue = CI-41; white = CI-56). We also show the stress inversion obtained by Holt *et al.* [2013] for the four clusters. Stereonets represent the horizontal plane (red = σ_1 ; green = σ_2 ; blue = σ_3 ; black dotted line = S_{Hmax}).

Holocene river gravels that hide any existence of past fault activity. These alluvial gravels are the youngest of the several overlapping fans of glacier rivers descending from the Southern Alps (Figure 1), which have produced the Canterbury Plains since Late Cretaceous [Forsyth *et al.*, 2008, and references therein]. The cover sequence consists of terrestrial-marine sedimentary units accumulated to over 1 km thickness [Ghisetti and Sibson, 2012] and obscuring the geomorphic expression of slow slip rate active faults crossing the plains such as the Greendale Fault [Van Dissen *et al.*, 2011]. Nor was the Greendale Fault identified by previous seismic reflection studies [e.g., Jongens *et al.*, 2012]. Alluvial sediments derive from Mesozoic greywacke rocks composing the Southern Alps and represent deposition during episodic glacial and interglacial periods [e.g., Barnes, 1995]. They include interlayered formations of gravels and fine to very fine grained sediments [e.g., Moar and Gage, 1973; Browne and Naish, 2003]. Their thickness reaches 1.5 km across the 160 km long and 50 km wide Canterbury Plains [Guidotti *et al.*, 2011]. Thickness variations have been ascribed to syn-rift deposition along the Gondwana margin during Late Cretaceous–Paleocene, with rifting imposing an extensive fault fabric within the basement [Laird and Bradshaw, 2004]. These inherited fault systems were reactivated during Neogene shortening [Sibson *et al.*, 2011]. The basement consists of Mesozoic metamorphic rocks (Torlesse composite terrane) largely outcropping in the mountains, which have undergone an intense polyphase deformation (Figure 1) [e.g., MacKinnon, 1983]. Finally, Banks Peninsula is characterized by Late Miocene basaltic volcanism [e.g., Herzer, 1979; Sewell, 1988; Hampton and Cole, 2008].

3. Data and Ground Motion Polarization Analysis

3.1. Data Set

Following the Darfield earthquake, Victoria University of Wellington, together with the University of Auckland and the University of Wisconsin-Madison, deployed a temporary network of 14 stations which recorded aftershocks during the period 8 September 2010 to 13 January 2011, of which over 2800 were located [Syracuse *et al.*, 2012, 2013]. The majority of these stations were installed on the flat Canterbury Plains (Figure 1), which have sediment thicknesses varying slowly between 0.5 and 1.5 km [Ghisetti and Sibson, 2012; Savage *et al.*, 2013]. We add data recorded by three broadband permanent GNS Science stations (CRLZ, MQZ, and OXZ).

Across the 25 km length of the Greendale Fault, the basement changes depth by less than 0.5 km [Ghisetti and Sibson, 2012], for an average slope of 1° . Holt *et al.* [2013] selected 2815 earthquakes and analyzed focal mechanisms and anisotropy. Well-resolved stress inversions were determined from 56 clusters of earthquakes. All shear wave splitting measurements reported were measured within the shear wave window, a cone of about 35° from the vertical; outside of which, conversions from *S* to *P* can interfere with the measurements [Crampin and Booth, 1985]. Corrections for angle of incidence due to surface topography and basement dip are negligible. Focal mechanisms mostly indicated strike-slip motion and a relatively uniform, strike-slip stress regime across the Canterbury Plains. Syracuse *et al.* [2013] also found that most of seismicity occurred at shallow depths (3–15 km) and along eight distinct fault segments. We select four clusters comprising 163 earthquakes, whose location is shown in Figure 1. This selection was determined to investigate possible variations of polarization in relation to the seismic source and path. The green cluster [CI-2 in Holt *et al.*, 2013] is located in the Rolleston faults [Syracuse *et al.*, 2013] at the eastern edge of the Greendale Fault. It is a broad area of intense seismicity where focal mechanisms indicate predominant left-lateral motion and minor evidence of horizontal extension. It is almost directly under station Dar5, so all its earthquakes are within a very strict interpretation of the shear wave window for a straight-line path (i.e., assuming a homogeneous medium with no bending in the top layers) at station Dar5. The red cluster (CI-4) lies on the N-S trending Kirwee fault [Syracuse *et al.*, 2013], which extends 18 km from the Greendale Fault to the North. The Kirwee fault crosses the hypocenter of Darfield 3 September earthquake and experienced left-lateral motion. The blue cluster (CI-41) is located on the main Greendale Fault with right-lateral strike-slip motion and is almost directly underneath station Dar6. The white cluster (CI-54) is located in the Eastern Hororata Fault [Beavan *et al.*, 2011, 2012; Syracuse *et al.*, 2013], which represents the westernmost fault segment. Focal mechanisms indicate mainly reverse motion with minor strike-slip components.

Considering that in the analysis we used aftershocks with magnitudes between 1.8 and 4.8, with the majority less than magnitude 3.0, we have decided to follow the common practice of neglecting directivity, as well as any near-field effects. There is not much literature on the effects of rupture directivity on small earthquakes [e.g., Kane *et al.*, 2013, is one of the few ones to look at these effects on small earthquakes]. Using the scaling relations of Hanks and Bakun [2002, 2008], fault areas for earthquake magnitude from 2 to 4.8 would range from 0.01 to 6.6 km^2 . Earthquake depths are almost all between 5 and 10 km, and so are at least 5 km from the sources. Finally, the average wavelengths are 0.8 km, calculated from the dominant frequency of 3 Hz [Holt *et al.*, 2013] and the surface velocity of 2.5 km/s [Syracuse *et al.*, 2013]. We thus conclude that these small earthquakes are also not likely to be affected much by directivity since their rupture length is small compared to their wavelength, and not in the near field since their wavelengths are small compared to the distance to the stations. We thus conclude that the earthquakes are small enough to be treated as point sources.

3.2. Polarization Analysis Method

The polarization analysis is performed on the data set previously described. Before proceeding with the analysis, signals are detrended and the mean is removed, and then they are tapered through a Hanning window for the spectral analysis. We study periods shorter than the natural period of the sensor, and tests showed little variation between raw and instrument-corrected data for the period ranges we investigated. Therefore, we present results without instrumental correction applied.

We determine the wavefield polarization through the method of analysis proposed by Pischiutta *et al.* [2012], which is performed in the frequency domain by computing the horizontal-to-vertical spectral ratios (HVSRS) after rotating the horizontal components in the azimuth range 0° – 180° , and in the time domain through diagonalization of the covariance matrix [Kanasewich, 1981; Jurkevics, 1988]. The 0° and 180° azimuths correspond to geographic North and South, respectively. To evaluate directional amplification and horizontal ground motion polarization, we combine results from these two methods of analysis. The HVSRS computation allows us to (i) identify the frequency band where directional amplification occurs and (ii) use the amplitude levels to give an indication of the effective strength (amplitude should be higher than 2.5, meaning that the horizontal component is more than 2.5 times as large as the vertical component for the peak under consideration). The covariance matrix analysis allows us to (i) study polarization trends along signals (seismic phases or ambient noise), (ii) better detect polarization directions, and (iii) observe the persistency of the effect on earthquakes with different sources/paths by evaluating the standard deviation of the circular histogram.

The use of spectral ratios after rotation of the horizontal components was first introduced by *Spudich et al.* [1996], to investigate possible directional effects in the horizontal plane. HVSRs show to what extent horizontal motions are amplified, compared to the vertical one, as a function of frequency and direction of motion. The time windows used for the spectral analysis start from the *P* waves and include the *S* and coda waves. After computing the fast fourier transform, amplitude spectra of the vertical and horizontal components are smoothed with a running 0.1 Hz wide rectangular box. The HVSR values are calculated from 0° to 180° at bins of 10°.

As an example of the polarization analysis, in Figure 2 we show results obtained from a M 3.0 earthquake (#3406724 in Table 1, from cluster 2) recorded at station Dar6. Spectral ratios reveal an amplitude 6 peak in the frequency band 3–4 Hz. The unfiltered three-component seismic records are depicted in the second panel and the filtered ones in the third panel.

In order to obtain a further estimate of the ground motion polarization we apply the covariance matrix method [Kanasewich, 1981; Jurkevics, 1988] in the time domain. We bandpass filter seismograms in the frequency band where the spectral peaks are observed, which is 1–6 Hz at most stations. An exception is made for stations Dar5, Cch2, and CRLZ for which we filter signals in the frequency bands 4–7 Hz, 6–9 Hz, and 3–6 Hz, respectively. The covariance matrix is computed along the filtered signals, beginning a few seconds before the *P* wave arrival and including the late coda. A 0.5 s long sliding window with 0.1 s overlap is run throughout the seismograms; in each window the polarization ellipsoid is estimated through the eigenvalues and eigenvectors of the covariance matrix by solving the algebraic eigenvalue problem. The eigenvalues and eigenvectors correspond, respectively, to the length and orientation of the polarization ellipsoid, thus defining the polarization vector in 3D. According to *Jurkevics* [1988], the polarization ellipsoid is characterized by three parameters: the rectilinearity “*R*” (varying from 0 for circular particle motions to 1 for purely rectilinear ones), the angle “*I*” of the largest eigenvector from the vertical axis, and the polarization angle “*AZ*” in the horizontal plane (measured from North). In order to give the most importance to time windows associated with more horizontal and elongated polarization ellipsoids, we apply the hierarchical criterion previously proposed by *Pischiutta et al.* [2012] and subsequently exploited by *Pischiutta et al.* [2013, 2014]. We thus define four classes of increasing reliability based on *R* and *I* values: we exclude from statistics values of *AZ* for which $R < 0.5$ and $I < 45^\circ$, and linearly normalize between 0 and 1 the *R* and *I* values ranging in the intervals $0.5 < R < 1$ and $45^\circ < I < 90^\circ$, making linearized values R_l and I_l . The weighted value in each time window is obtained from the product $WH = R_l * I_l$; thus, $0 < WH < 1$. *WH* is then used as a weight for the horizontal *AZ* values contributing to the rose diagrams of horizontal polarization.

An example time domain analysis is given in the fourth panel of Figure 2. On the top of the fourth panel we plot polarization azimuth values versus time, using a color scale related to *WH* associated with each time window (black to light blue, as indicated in the figure). We select eight time windows (thus polarization azimuth values) along the signals related to different seismic phases, in order to show some examples of different shape (elongation, horizontality, and flatness) of the polarization ellipsoid depending on values of reliability. In order to show the influence of the appliance of this hierarchical criterion on the final representation of ground motion azimuth results, we finally show two rose diagrams representing polarization azimuth graphed from 0° to 360°, at bins of 10°. The “HC” rose diagram is made by applying the hierarchical criterion; thus, each polarization azimuth value contributes to statistics in a percentage defined by its associated *WH* value; conversely, the “NO-HC” one is produced, inserting polarization azimuth values with the same weight (1).

3.3. Results From Seismic Events

As a first step we calculate the HVSRs separately for each event-station pair. Then at each station the geometric mean is computed over the available events and spectral ratios are derived from the averages over all the seismic events used. Results at each station are illustrated in Figure 3. A recurrent peak of HVSR at very low frequencies (between 0.1 and 0.3 Hz) is evident at stations installed in the sedimentary basin (Cch4, Cch1, Cch2, Dar2, Dar3, Dar4, Dar5, Dar6, Dar7, and Dar8), with HVSR amplitudes exceeding a factor of 2. Amplitudes do not change much with the rotation angle (Figure 3). This low-frequency peak is absent on stations on Banks peninsula (Bnk1, CRLZ, and MQZ) and at OXZ where rocks outcrop. An exception is station Dar1: even though it is installed in the sedimentary basin [as determined by the geological map of *Ghisetti and Sibson*, 2012], this station does not show the previously mentioned low-frequency peak.

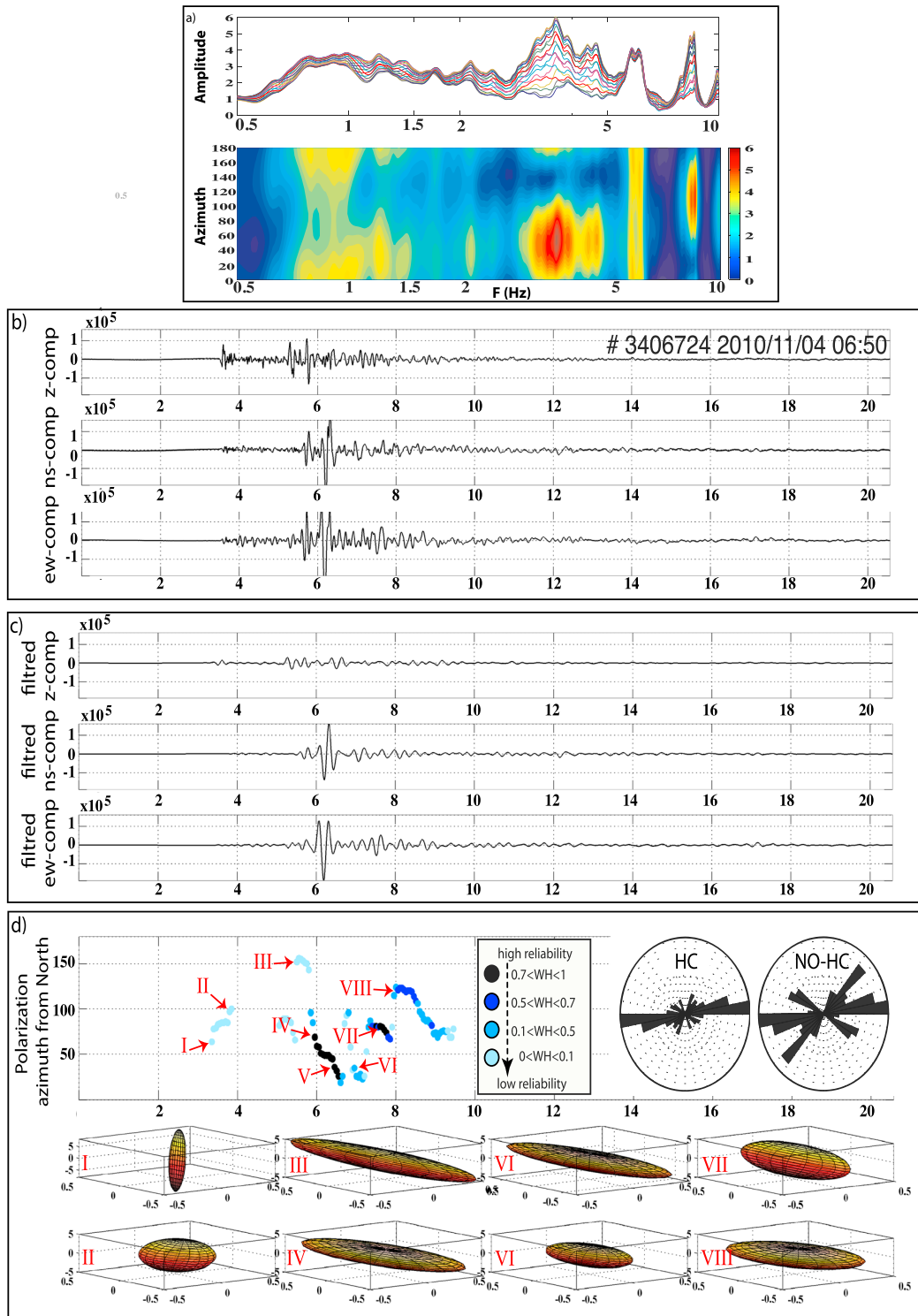


Figure 2. Example of horizontal polarization analysis performed using one earthquake (#3406724 in Table 1). (a) HVSRs calculated over the entire seismogram length. In the top panel, average spectral ratios are drawn separately for rotation angle from 0° to 180° . In the bottom panels the same spectral ratios are shown in a color contour representation: the y axis and x axis represent rotation angle and frequency, respectively, and the color scale quantifies the H/V amplitudes; (b) unfiltered three-component waveforms; (c) three-component waveforms filtered in the frequency band 1–6 Hz, where the amplification effect is evident in the HVSRs; and (d) details of the wavefield polarization analysis. The polarization ellipsoids drawn at the bottom are representative of different time windows and seismic phases as seen in the seismograms above. Their shape is indicative of the reliability class associated to the time window they belong to, with longer axes indicating higher reliability. The polarization azimuth values are colored following the assigned reliability class. Azimuth values are also represented as rose diagram obtained with (HC) and without (NO_HC) the appliance of the hierarchical criterion.

Table 1. Dataset Used for the Analysis

Cuspid	Latitude	Longitude	Depth	Year	Month	Day	Hour	Minute	Second
<i>Cluster 2</i>									
3371554	−43,558,243	172,431,191	10,954	2010	9	13	11	7	34.91
3371710	−43,558,544	172,415,495	12,669	2010	9	13	18	34	6.75
3372899	−43,576,876	172,405,135	7,293	2010	9	16	2	21	9.00
3373646	−43,537,107	172,435,700	8,020	2010	9	17	10	5	45.61
3374575	−43,573,308	172,443,235	14,141	2010	9	19	2	14	49.92
3375800	−43,558,980	172,453,988	7,124	2010	9	21	5	5	3.94
3376090	−43,560,358	172,438,157	11,351	2010	9	21	18	50	29.88
3376566	−43,555,585	172,417,677	9,898	2010	9	22	15	27	34.00
3376639	−43,551,031	172,441,233	9,900	2010	9	22	18	22	25.73
3376732	−43,550,927	172,439,657	10,305	2010	9	22	22	24	30.69
3376993	−43,554,248	172,442,528	10,383	2010	9	23	8	19	28.72
3378613	−43,559,346	172,443,208	10,872	2010	9	26	6	9	21.76
3384281	−43,544,743	172,429,655	6,874	2010	10	7	15	40	43.60
3386411	−43,529,797	172,427,665	7,918	2010	10	11	15	0	55.94
3387281	−43,551,930	172,424,460	7,037	2010	10	12	9	33	13.75
3387496	−43,557,448	172,439,501	6,366	2010	10	12	20	27	55.96
3388817	−43,551,130	172,441,148	9,886	2010	9	22	18	22	25.06
3388937	−43,557,038	172,438,437	6,300	2010	10	14	1	51	51.83
3394421	−43,559,248	172,436,110	7,479	2010	10	23	17	44	43.87
3394865	−43,542,228	172,419,731	8,423	2010	10	24	16	20	34.73
3400620	−43,563,514	172,418,231	7,282	2010	11	1	6	19	54.83
3401272	−43,550,200	172,428,017	6,786	2010	11	2	14	36	21.73
3402024	−43,555,421	172,430,861	9,352	2010	11	4	1	35	52.57
3402144	−43,548,519	172,422,984	9,041	2010	11	4	6	50	45.84
3406724	−43,553,723	172,428,539	9,934	2010	11	13	13	10	44.05
3406855	−43,554,073	172,429,790	9,970	2010	11	13	19	38	46.72
3407078	−43,556,741	172,427,039	9,243	2010	11	14	6	21	5.07
3407087	−43,551,740	172,426,276	9,646	2010	11	14	6	42	43.85
3407093	−43,554,144	172,428,768	9,807	2010	11	14	6	56	45.79
3407143	−43,551,393	172,428,476	9,963	2010	11	14	9	14	2.92
3407152	−43,552,409	172,426,605	10,273	2010	11	14	6	58	46.78
3407383	−43,559,230	172,433,643	11,031	2010	11	14	7	1	46.74
3407403	−43,555,363	172,431,511	9,261	2010	11	14	21	56	48.84
3407405	−43,555,536	172,431,329	9,401	2010	11	14	22	1	6.80
3407521	−43,554,871	172,433,343	9,245	2010	11	13	12	35	42.92
3407827	−43,511,778	172,398,574	1,323	2010	11	15	18	42	36.66
3407827	−43,569,919	172,403,721	5,105	2010	11	15	18	42	37.06
3408645	−43,558,152	172,430,700	10,598	2010	11	17	8	53	3.78
3411965	−43,560,273	172,439,464	10,942	2010	9	18	18	29	17.79
3413135	−43,548,958	172,438,772	10,086	2010	11	26	11	29	35.02
3421300	−43,561,868	172,432,141	11,289	2010	12	13	18	51	12.79
3429569	−43,551,042	172,436,517	11,043	2010	12	18	12	27	43.88
3429697	−43,551,631	172,435,354	11,024	2010	12	18	19	9	17.84
3432134	−43,557,001	172,447,488	7,319	2010	12	21	16	3	31.76
3436443	−43,561,176	172,434,216	11,572	2010	12	24	9	54	39.95
3439223	−43,542,452	172,417,222	7,485	2010	12	30	7	56	55.75
<i>Cluster 4</i>									
3369962	−43,461,025	172,158,612	7,862	2010	9	10	7	29	46.75
3370661	−43,471,797	172,123,655	10,912	2010	9	11	17	18	7.69
3370894	−43,499,732	172,161,934	9,321	2010	9	12	4	24	37.75
3371392	−43,464,346	172,167,103	6,695	2010	9	13	3	35	11.74
3372040	−43,460,796	172,157,744	7,996	2010	9	14	10	16	57.74
3372169	−43,463,034	172,153,408	7,527	2010	9	14	16	27	38.68
3372344	−43,467,539	172,144,121	10,123	2010	9	15	1	9	27.58
3373006	−43,499,056	172,176,901	6,307	2010	9	16	6	55	10.60
3373081	−43,487,535	172,123,152	10,521	2010	9	16	10	33	40.70
3373252	−43,492,012	172,183,157	8,104	2010	9	16	17	54	4.76
3373495	−43,484,824	172,124,508	9,416	2010	9	17	3	37	22.90
3374000	−43,504,654	172,160,962	10,415	2010	9	18	1	19	11.98
3374615	−43,443,472	172,146,717	8,999	2010	9	19	4	0	16.75

Table 1. (continued)

Cuspid	Latitude	Longitude	Depth	Year	Month	Day	Hour	Minute	Second
3374974	−43,488,353	172,123,805	10,351	2010	9	19	19	58	26.89
3375210	−43,451,078	172,157,280	7,621	2010	9	20	5	17	57.83
3376195	−43,461,050	172,144,687	6,718	2010	9	21	23	39	35.77
3382671	−43,472,020	172,168,696	7,062	2010	10	4	9	6	16.80
3383302	−43,462,433	172,153,308	7,303	2010	10	5	16	18	38.77
3384228	−43,460,128	172,143,418	6,691	2010	10	7	13	39	13.47
3389560	−43,481,228	172,161,854	8,277	2010	10	15	8	27	4.83
3391095	−43,491,926	172,150,610	9,774	2010	10	18	9	22	13.57
3392200	−43,472,481	172,165,989	6,647	2010	10	19	6	30	53.76
3392249	−43,481,165	172,161,427	8,315	2010	10	19	9	7	11.67
3392480	−43,443,434	172,141,674	10,157	2010	10	19	21	9	26.67
3395251	−43,466,448	172,160,230	6,810	2010	10	25	12	15	52.80
3398153	−43,488,249	172,123,496	10,175	2010	10	28	16	51	59.81
3398198	−43,472,192	172,166,789	6,882	2010	10	28	9	35	34.72
3399302	−43,469,906	172,167,756	7,105	2010	10	29	12	42	22.81
3399694	−43,471,659	172,168,101	6,954	2010	10	30	9	4	51.79
3399970	−43,443,273	172,139,955	9,137	2010	10	30	22	26	52.72
3402581	−43,472,364	172,166,459	6,745	2010	11	5	5	34	12.83
3410317	−43,477,963	172,158,486	7,484	2010	11	20	17	1	27.59
3412167	−43,459,321	172,151,486	6,814	2010	11	24	13	33	14.80
3412292	−43,464,759	172,155,778	6,211	2010	11	24	19	52	19.75
3413204	−43,465,903	172,140,494	8,269	2010	11	26	15	0	28.90
3417662	−43,462,078	172,158,083	7,722	2010	9	26	11	16	28.88
3434856	−43,452,215	172,148,563	7,480	2010	12	22	0	44	4.86
<i>Cluster 41</i>									
3369944	−43,584,603	172,235,332	7,092	2010	9	10	6	39	42.60
3370015	−43,587,411	172,257,990	10,646	2010	9	10	9	32	13.90
3370443	−43,595,111	172,245,721	9,922	2010	9	11	6	8	42.91
3370461	−43,571,877	172,260,552	14,116	2010	9	11	7	8	23.90
3370754	−43,595,543	172,256,077	9,783	2010	9	11	21	49	59.80
3371448	−43,580,016	172,225,511	6,718	2010	9	13	5	59	54.79
3371575	−43,592,443	172,250,037	6,134	2010	9	13	12	7	46.86
3371644	−43,593,362	172,242,773	9,702	2010	9	13	15	16	24.92
3372395	−43,579,526	172,261,468	8,959	2010	9	15	3	11	26.22
3372533	−43,584,959	172,242,033	7,024	2010	9	15	9	24	25.43
3372593	−43,593,139	172,244,146	9,897	2010	9	15	12	15	14.28
3372927	−43,591,010	172,257,726	9,360	2010	9	16	3	23	49.04
3374044	−43,593,404	172,240,344	10,444	2010	9	18	3	13	33.77
3374699	−43,599,788	172,244,492	10,185	2010	9	19	7	20	14.90
3374885	−43,596,945	172,248,479	11,510	2010	9	19	15	49	8.93
3376421	−43,589,709	172,243,917	11,522	2010	9	22	9	21	33.97
3376671	−43,578,327	172,259,894	7,259	2010	9	22	19	59	43.24
3377119	−43,592,657	172,256,712	8,894	2010	9	23	14	23	28.03
3377340	−43,595,854	172,235,578	9,444	2010	9	24	0	3	58.24
3377627	−43,583,813	172,236,720	9,338	2010	9	24	11	10	31.01
3377863	−43,590,490	172,257,858	8,562	2010	9	24	20	37	58.27
3378176	−43,616,179	172,245,409	8,989	2010	9	25	10	14	26.28
3378788	−43,594,667	172,233,343	8,906	2010	9	26	13	56	30.09
3379093	−43,584,440	172,251,207	8,361	2010	9	27	4	43	4.27
3380326	−43,587,505	172,240,189	7,528	2010	9	29	14	58	36.67
3381485	−43,595,431	172,255,732	8,707	2010	10	1	23	23	4.61
3381640	−43,583,672	172,255,365	7,891	2010	10	2	7	8	17.09
3382741	−43,592,590	172,262,770	8,963	2010	10	4	12	31	37.91
3383597	−43,600,058	172,252,374	11,761	2010	10	6	6	12	31.91
3383984	−43,594,900	172,249,175	10,735	2010	10	7	1	40	34.92
3384007	−43,588,649	172,251,334	6,325	2010	10	7	2	40	54.82
3389856	−43,572,121	172,261,202	14,291	2010	10	16	0	7	29.81
3402340	−43,590,790	172,233,386	7,766	2010	11	4	17	36	44.11
3403127	−43,596,618	172,241,837	10,694	2010	11	6	9	7	51.51
3406534	−43,607,352	172,253,390	8,428	2010	11	13	3	15	2.98
3407384	−43,587,738	172,238,987	11,473	2010	11	14	21	6	43.00

Table 1. (continued)

Cuspid	Latitude	Longitude	Depth	Year	Month	Day	Hour	Minute	Second
3411056	−43,610,407	172,250,033	9,077	2,010	11	22	8	22	37.35
3412435	−43,586,119	172,232,811	7,612	2,010	11	24	12	2	9.36
3412914	−43,588,276	172,235,161	6,620	2,010	9	19	8	41	37.87
3413849	−43,593,608	172,243,440	8,637	2010	11	28	0	13	58.74
3418998	−43,605,110	172,237,048	8,837	2010	9	24	2	41	8.26
3443542	−43,587,125	172,234,381	7,335	2010	12	12	23	56	24.95
<i>Cluster 54</i>									
3369807	−43,519,528	171,864,544	11,399	2010	9	10	0	57	31.05
3370040	−43,536,944	171,859,858	9,793	2010	9	10	10	36	41.96
3370088	−43,526,064	171,881,386	8,825	2010	9	10	12	46	38.69
3370475	−43,529,565	171,873,208	10,545	2010	9	11	7	53	16.72
3370670	−43,525,725	171,896,138	11,374	2010	9	11	17	44	29.10
3370794	−43,518,892	171,864,733	11,449	2010	9	11	23	39	9.58
3371678	−43,535,051	171,871,053	8,352	2010	9	13	16	54	0.03
3371991	−43,522,311	171,887,075	9,725	2010	9	14	8	2	59.37
3372524	−43,521,421	171,857,163	11,206	2010	9	15	8	53	45.02
3374113	−43,535,338	171,843,924	9,154	2010	9	18	5	57	33.98
3374132	−43,516,393	171,860,995	8,920	2010	9	18	6	48	58.85
3374895	−43,521,426	171,873,772	9,475	2010	9	19	16	14	34.03
3375395	−43,513,355	171,858,923	8,524	2010	9	20	12	44	30.98
3375833	−43,523,179	171,891,826	7,264	2010	9	21	6	28	7.57
3375993	−43,544,306	171,866,584	7,741	2010	9	21	14	20	49.80
3376420	−43,519,979	171,892,773	6,877	2010	9	22	9	18	50.56
3377037	−43,515,841	171,872,854	10,063	2010	9	23	10	25	9.51
3377039	−43,528,019	171,872,853	10,299	2010	9	23	10	34	1.15
3377096	−43,534,643	171,875,679	8,721	2010	9	23	13	17	23.26
3377204	−43,515,269	171,869,604	10,810	2010	9	23	18	10	42.24
3378933	−43,534,770	171,875,103	8,731	2010	9	26	20	53	25.41
3381629	−43,527,973	171,871,802	10,171	2010	10	2	6	40	33.04
3382247	−43,510,069	171,877,165	7,984	2010	10	3	13	13	44.82
3383037	−43,537,209	171,897,326	7,397	2010	9	10	7	12	17.69
3383353	−43,538,210	171,846,880	9,069	2010	10	5	18	47	37.02
3384190	−43,530,619	171,862,067	8,555	2010	10	7	11	8	12.87
3384261	−43,544,630	171,873,528	8,152	2010	10	7	14	36	7.03
3384665	−43,529,175	171,872,250	9,711	2010	10	8	10	8	51.93
3384666	−43,529,561	171,872,923	9,759	2010	10	8	10	13	10.13
3386123	−43,516,321	171,873,346	10,527	2010	9	11	6	30	44.97
3387551	−43,550,493	171,866,128	5,979	2010	10	12	23	17	43.77
3394643	−43,524,301	171,875,364	9,494	2010	10	24	5	35	15.12
3396469	−43,522,304	171,877,136	9,536	2010	10	27	21	1	46.01
3400023	−43,525,764	171,894,868	7,329	2010	10	31	1	4	54.87
3401516	−43,524,472	171,868,943	9,978	2010	9	15	14	12	1.01
3402177	−43,538,597	171,854,835	7,406	2010	11	4	8	44	10.94
3402224	−43,538,598	171,855,667	7,405	2010	11	4	11	24	55.06
3407481	−43,524,743	171,874,724	9,506	2010	10	24	4	10	50.95
3429940	−43,526,689	171,880,730	8,448	2010	12	19	8	6	36.01

Another frequency band, between 2 and 5 Hz, shows horizontal amplification. This is observed most strongly at stations installed within tens of meters from the fault (Dar4, Dar6, Dar7, and Dar8). Horizontal motions tend to exceed the vertical one with HVSr amplitudes up to a factor of 3.5. In contrast to the isotropic amplification effect recognized at low frequency, HVSrs of the frequency band 2–5 Hz at these stations are amplified mostly along a specific azimuth, which forms a high angle with the E-W trending fault segment (maximum variation between azimuths at these stations is a factor of 2 in this frequency band). In the same frequency band, two stations (Cch1 and Cch4) show spectral peaks up to a factor of 3 that are more equally distributed over the rotation angles (maximum variation of 0.5 between azimuths in this frequency band). The remaining stations (ChT2, CRLZ, Dar2, Dar3, Dar5, and MQZ) do not show significant amplification effects, HVSr amplitudes being lower than 2 at frequencies higher than 1 Hz. Finally, at stations OXZ and Dar1, the HVSr curves reach an amplitude of 2.7, with spectral peaks at 1 Hz and 2 Hz, respectively. They both show a

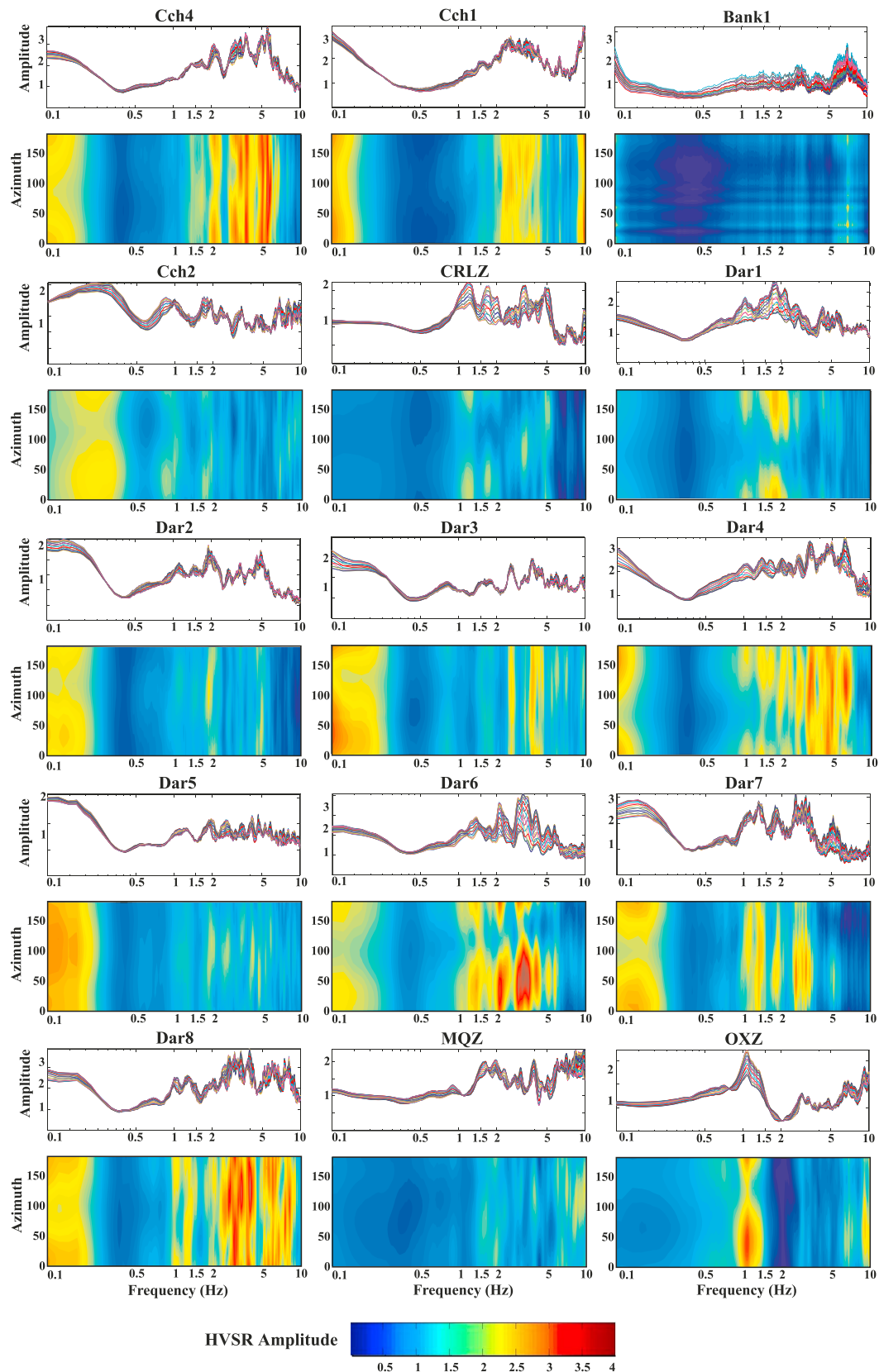


Figure 3. Average horizontal-to-vertical spectral ratios of stations. The geometric mean is computed over the ensemble of analyzed seismic events. The representation is the same as that in Figure 2a.

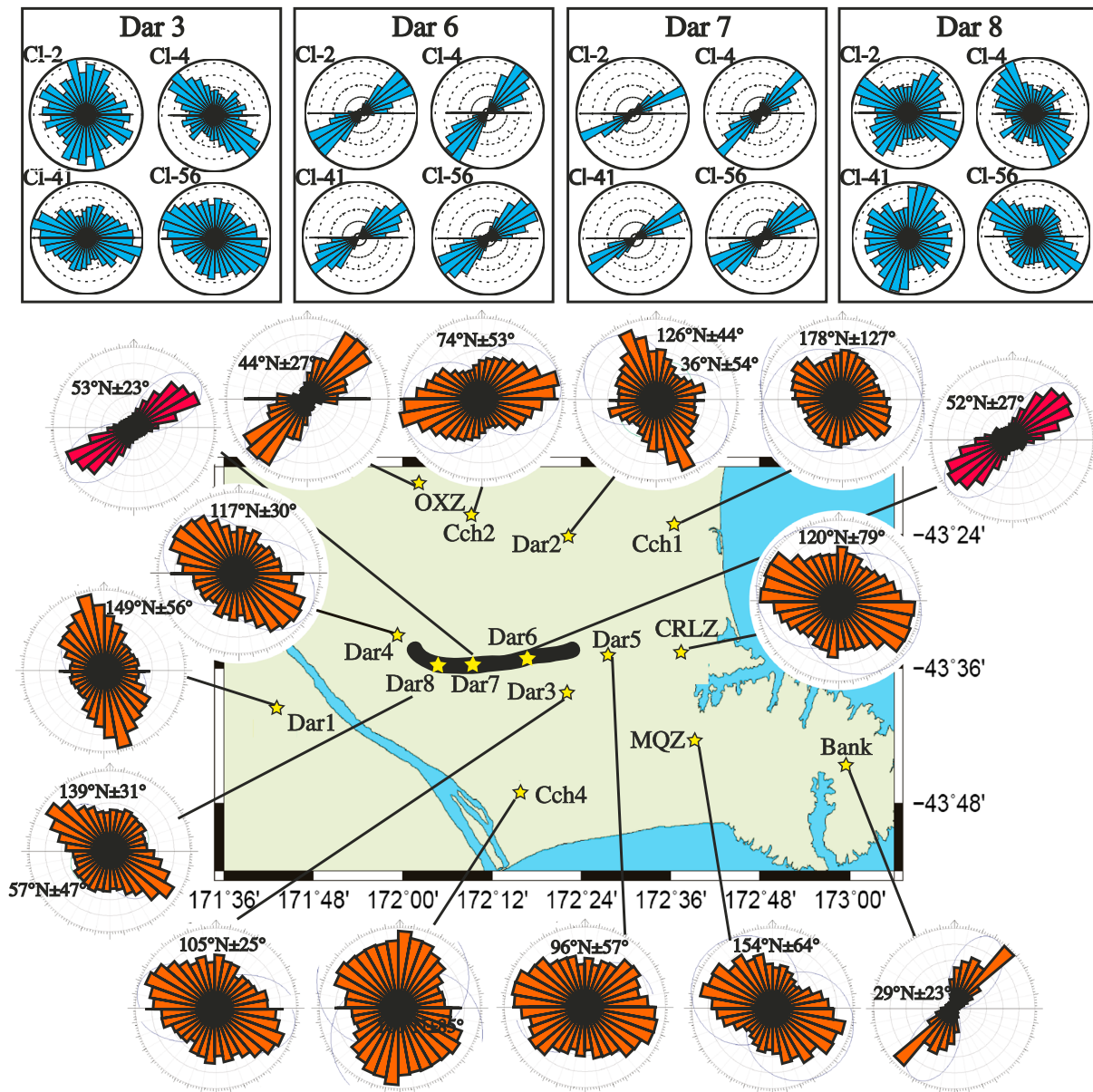


Figure 4. Horizontal polarization at each station obtained by analyzing earthquakes selected among four clusters. The black line represents the morphological signature of the Darfield main rupture [Van Dissen et al., 2011]. The top insets show horizontal polarization at four selected stations for the different clusters (CI-2, CI-4, CI-41, and CI-56): each cyan rose diagram is obtained by aggregating polarization results of earthquakes belonging to the same cluster. The orange circular histograms in the main figure are obtained by aggregating results of the whole data set.

directional amplification effect. Even though the amplified frequency band is station dependent, we observe a common tendency of stations to show amplification in the band 2–5 Hz. Thus, we bandpass signals in the frequency band 1–6 Hz before proceeding with the covariance matrix analysis in the time domain. The analysis is repeated for all of the events of the four selected clusters, and then we aggregate the polarization azimuths of each station for the whole data set. We finally produce a circular histogram for each station where the statistical contribution to each polarization azimuth value is defined by its associated value of WH ($0 < WH < 1$), which depends on polarization ellipsoid shape (rectilinearity and elongation), as explained in section 3.2.

The pattern of horizontal ground motion inferred from the covariance matrix analysis is shown in Figure 4 together with the Darfield strike-slip fault. In order to estimate the mean and the standard deviation of the

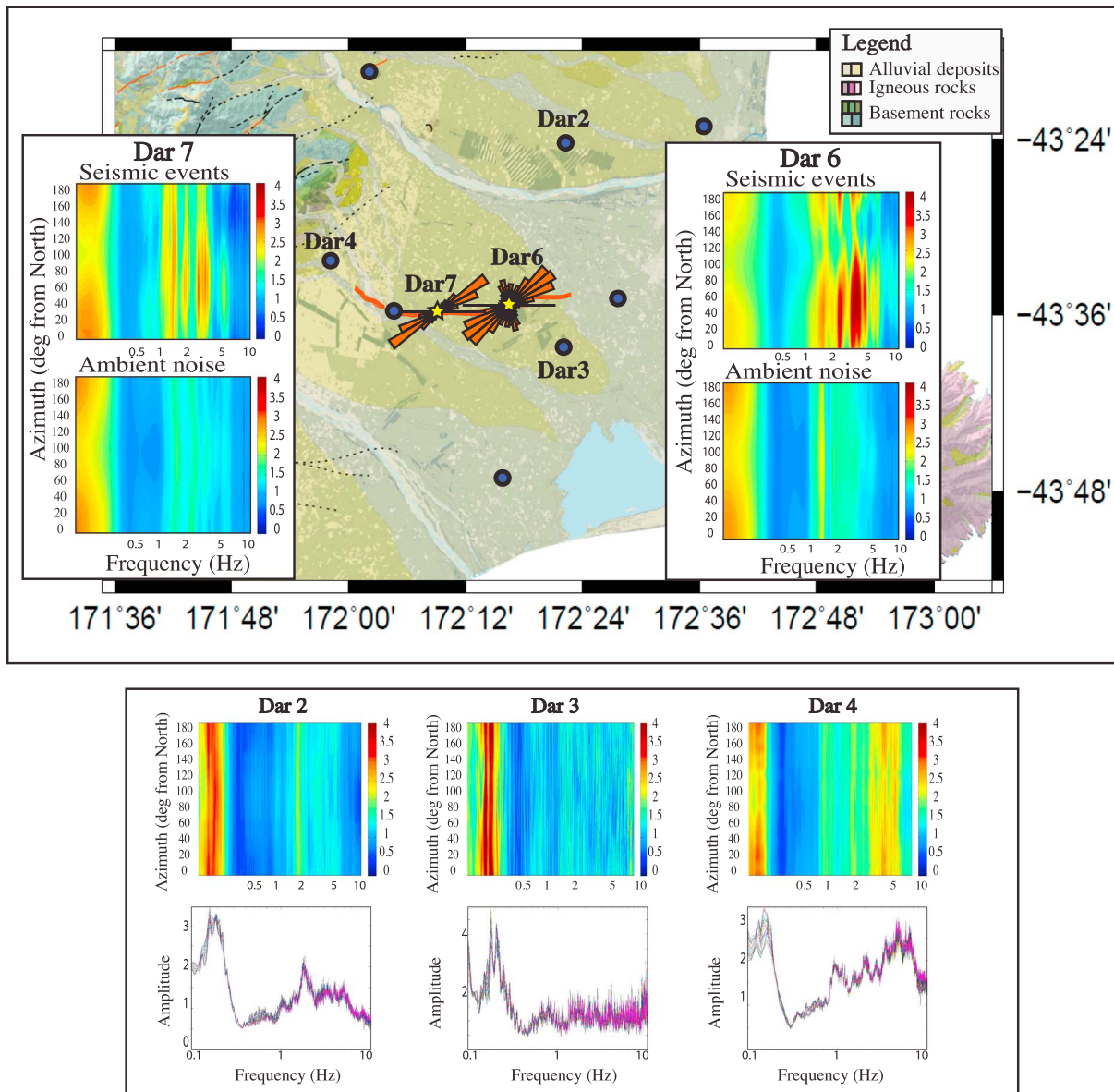


Figure 5. (top) Horizontal-to-vertical spectral ratios calculated at on-fault stations Dar6 and Dar7 on ambient noise and as an average of the analyzed seismic events. The orange rose diagrams represent, as in Figure 4, the horizontal polarization calculated on the whole data set, bandpass filtering data from 1 to 6 Hz. (bottom) Horizontal-to-vertical spectral ratios calculated at stations Dar2, Dar3, and Dar4 on ambient noise.

polarization, circular histograms are fit with a Gaussian curve using the Daisy Package [Salvini *et al.*, 1999, available at <http://host.uniroma3.it/progetti/fralab/>]. The mean direction of the horizontal polarization as well as the standard deviation is listed in Figure 4. Two stations installed on the fault, Dar6 and Dar7, show narrow rose diagrams peaked in $N52^\circ \pm 27^\circ$ and $N53^\circ \pm 24^\circ$ directions, respectively (red rose diagrams in Figure 4), which result from consistent polarization of the analyzed clusters of seismic events (cyan rose diagrams on the top of Figure 4). The other station installed on the fault, Dar 8, has highly complex results, with polarization being much more affected by the seismic path. All the other stations installed in the Canterbury Plains and at distances in the order of kilometers from Greendale Fault (Dar1, Dar2, Dar3, Dar4, Dar5, Cch1, Cch2, Cch4, CRLZ, and MQZ) show very scattered rose diagrams, with ground motion showing no horizontal polarization (orange rose diagrams in Figure 4). Station OXZ is the exception, exhibiting a polarization effect consistent with the two on-fault stations, as previously mentioned. Also, station Bank shows a polarization rose diagram peaked at $N29^\circ \pm 23^\circ$, but because the HVSR amplitude is lower than 2 we do not consider this station to be affected by directional amplification.

3.4. Results From Ambient Noise

In order to check the role of the sedimentary deposits beneath many stations, we repeat the spectral analysis using ambient noise that was continuously recorded for 72 days after 19 September 2010. For each day we select 1 h during night time (from 4 to 5 AM) to minimize the influence of cultural sources. Before the horizontal-to-vertical noise spectral ratio (HVNSR) computation we eliminate nonstationary disturbances using the antitrigger algorithm proposed in the SESAME (site effects assessment using ambient excitations —<http://sesame-fp5.obs.ujf-grenoble.fr/index.htm>) guidelines, in order to select the stationary parts to avoid transients associated with very close disturbances such as aftershocks, vehicles, and other kinds of cultural noise.

The analysis results are shown in Figure 5. In the top panel we compare the mean HVNSRs of ambient noise at on-fault stations Dar6 and Dar7 with the HVSRs derived from earthquakes. We observe that the directional amplification effect that is persistent on earthquake records at frequencies between 2 and 6 Hz disappears in the ambient noise analysis. Nevertheless, the amplification peak at (0.1–0.3 Hz) is also strong on the ambient noise. This low-frequency peak is isotropic, maintaining the same amplitude at all rotation angles. The same feature is found at other stations in the Canterbury basin. In the bottom panel of Figure 5 we show HVNSRs of stations Dar2, Dar3, and Dar4 using the same contour plot representation. The average spectral ratios for each rotation angle are drawn separately to better visualize the absence of amplitude variations at different azimuths. All stations show an amplitude 3–4 peak at low frequency.

4. Discussion

4.1. The Sedimentary Basin Resonance Effect

The Greendale Fault is buried under the Canterbury Plains, which are composed of poorly consolidated alluvial gravel with a considerable thickness (around 1 km) [e.g., *Ghisetti and Sibson*, 2012]. We consider that the presence of thick low-velocity soft sediments over the bedrock with higher velocity in the Canterbury sedimentary basin is responsible for the amplification effects that are observed on ambient noise and earthquakes at frequencies lower than 1 Hz (0.1–0.3 Hz in Figures 3 and 5). The isotropic peak of a factor of 3 at 2–5 Hz at stations Cch1 and Cch4 (Figure 3) might be caused by a second shallower velocity contrast in the sedimentary basin succession. *Savage et al.* [2013] carried out noise cross correlation of the same data set described in section 3.3 to calculate surface waves traveling between each set of stations. At periods of 1–3 s, radial-radial cross-correlation functions had energy traveling at speeds greater than 1.1 km/s. This peak was nearly absent in the vertical-vertical cross-correlation function, implying longitudinal motion and a high H/V ratio. A one-dimensional regional velocity model incorporating an ~1.5 km thick sedimentary layer fits both the observed H/V ratio and Rayleigh wave group velocity.

Surprisingly, the peak of 2.5 s, or 0.4 Hz, for the H/V ratio of this higher mode surface wave is not strong on the noise analysis here. Instead, a peak between 0.1 and 0.3 Hz (3–10 s) is observed in this study, which corresponds to the broad peak of 4–10 s of the fundamental mode in both the measured and synthetic seismograms in the *Savage et al.* [2013] surface wave propagation study. It thus appears that the H/V spectral ratio of the noise in this study is controlled dominantly by the fundamental mode of the surface waves in the area. The H/V ratio studied here is calculated for all waves (*P*, *S*, and surface waves) coming in at all azimuths to a single station, whereas the *Savage et al.* [2013] study was considering only surface waves traveling within limited velocity ranges and at given polarizations between stations. The *Savage et al.* [2013] study also found that Love waves arrived close in time to the Rayleigh waves, and that amplitudes of Love waves were similar regardless of azimuth, while Rayleigh waves were stronger on paths from the ocean. Synthetic models (not shown here) with the same parameters as those in the *Savage et al.* [2013] study also yield fundamental resonance of Love waves at 0.2 Hz with amplitude levels higher than 3. We therefore conclude that the H/V ratios measured here could be caused by higher excitation of Love waves compared to Rayleigh waves, as well as by amplification of the fundamental Rayleigh waves.

4.2. Directional Amplification in the Fault Damage Zone

In addition to the amplification at lower frequency, two on-fault stations (Dar6 and Dar7) show another amplitude 4 peak at higher frequencies (2–5 Hz; Figure 3). This effect is evident only when using seismic events for the analysis. In the supporting information we show that the high frequency peak is present in

the earthquake coda waves and is amplified at the same N50° azimuth, independently of focal mechanism, while the amplification from the *S* waves alone occurs at variable azimuths that depend on focal mechanism. Because the noise is likely caused by surface waves traveling long distances through the Canterbury basin, while the earthquake coda includes body and surface waves that have traveled a smaller distance, this suggests that rocks buried beneath the sediments near the stations cause this high frequency peak. This peak does not attain the same amplitude for all the azimuths, appearing strongly anisotropic with ground motion polarization occurring in the \approx N50° direction.

We finally stress that the 2–5 Hz peak around N50° direction is evident only at on-fault stations, suggesting a role of the fault damage zone. Fault damage zones [Caine *et al.*, 1996] are characterized by the presence of organized sets of brittle deformations and dilations (i.e., fracture systems or cracks) showing a predominant orientation. They are produced by the near-fault local stress field accumulated by friction during the fault activity [Riedel, 1929; Harding, 1974; Hobbs *et al.*, 1976; Harding and Lowell, 1979] and by its interaction with the tectonic stress field. Individual fractures can reach up to several meters with spacing down to one tenth of their dimension. They can include synthetic cleavages [i.e., R planes according to the definition by Riedel, 1929], antithetic cleavages (R' planes), extensional fractures (T planes), and pressure solution surfaces (P planes). One set is usually the most common because its development inhibits further significant elastic stress accumulation as well as the growth of other sets.

In order to interpret our finding, following Pischiutta *et al.* [2012, 2013], we model the fracture field associated with the Darfield fault damage zone, using the in-house software FRAP [Salvini *et al.*, 1999], which uses a combined numeric and analytic approach to determine fracture distribution patterns given fault zone physical parameters and kinematically related and/or dynamic fault slip values. The physical parameters chosen for the model are computed by averaging the values for the poorly consolidated sediments and the basement metamorphic rocks [Turcotte and Shubert, 1982]: density 2600 kg/m³, cohesion 5 MPa, Poisson ratio 0.25, friction angle 30°, and clay content 10%.

The model sensitivity was tested in Pischiutta *et al.* [2013] by varying the rheological parameters within realistic ranges, resulting in negligible strike variations (\approx 5°) of the predicted fracture patterns. This indicated that fracture type and orientation mostly depend on the acting stress.

According to the fault geometry in the investigated sector, the Greendale Fault is modeled as a near-vertical surface striking in the N85° direction (Figure 7) with dimensions 20 km (along strike) \times 9 km (along dip).

The fault surface is discretized into a grid of quadrangular cells of about 250 \times 60 m. The software computes the stress components in each cell, which include the overburden σ_v , the fluid isotropic pressure within the rock pores P_v (i.e., lithostatic at hydrostatic pressure, both linearly increasing with depth), the regional stress tensor σ_R , and the “kinematic stress” σ_K that represents the elastic stress accumulation due to frictional motion related to the fault activity.

We consider two models. In the first we model fracture distribution produced only by the fault kinematics, which is fixed to be purely right-lateral strike slip with a total displacement of 500 m. This value is chosen on the basis of fault dimension [Walsh and Watterson, 1988]. Consistent with the fault kinematics [e.g., Gledhill *et al.*, 2011], we orient the slip vector to N85° with 0° plunge, fault slip occurring parallel to the fault plane. The sum of all the stress components (σ_v , P_v , and σ_K) gives the resulting stress tensor σ_A , which is compared to the Coulomb-Navier Failure Criterion [Mandl, 2000]: fractures develop in a given cell of the model when the resulting stress tensor exceeds the strength. This model predicts that extensional fracture predominates with an average strike of N139° \pm 3.7° (Figure 7b). Standard deviation values are small because the model is analytic and not deterministic. Their azimuthal distribution is computed using the Daisy Package [Salvini *et al.*, 1999; available at <http://host.uniroma3.it/progetti/fralab/>], and their strike is visualized through a wind-rose diagram. Synthetic cleavage can also develop with an average strike of N101° \pm 3.6°. Secondly, antithetic cleavages and pressure solution surfaces are expected in N161° \pm 3.7° and N39° \pm 3.6° directions, respectively (see Table 2). The predominance of extensional fractures can be explained in terms of fluid pressure in the Quaternary basin that decreases the value of the effective stress (i.e., a left shift in the Mohr circle diagrams). This contrasts with results from other environments such as in the Hayward fault case study, where an orthogonal relation between the horizontal polarization and the predominant synthetic cleavage was found [Pischiutta *et al.*, 2012]. This discrepancy might be related to different geological contexts: in the

Table 2. Results From the Kinematic Stress Model^a

Kinematic Stress Model				
Fracture	Strike	Comparison With <i>Quigley et al.</i> [2010] Surface Rupture	Most Probable	Comparison With Seismic Observations
Extensional fracture (EF)	$139^\circ \pm 3.7^\circ$	NW-SE tension fractures	Depth < 2 km	Orthogonal relation with the horizontal polarization N52 ± 22° (Dar6) N53 ± 23° (Dar7)
Synthetic cleavage (SC)	$101^\circ \pm 3.6^\circ$	WNW-ESE Riedel (R) shear fractures	Depth > 2 km	Parallel relation with S wave fast component N100° ± 31° (Dar6)
Antithetic cleavage (AC)	$161^\circ \pm 3.7^\circ$	NNW-SSE Antithetic Riedel (R') shear fractures		
Pressure solution (PS)	$39^\circ \pm 3.6^\circ$	NE-SW folds/reverse faults		

^aFracture type and strike are compared with surface ruptures measured by *Quigley et al.* [2010]. The most probable fracture type is reported as well as the comparison with seismic observation (i.e., horizontal polarization and seismic anisotropy).

Canterbury basin the presence of fluids in recent sediments plays a significant role, decreasing the effective stress in the fault damage zone; in the San Andreas fault, on the other hand, erosional processes lift to the surface portions of the rocks that were deformed (fractured) at depths by the long-lasting San Andreas fault system.

In order to assess the reliability of the modeled fracture orientations, we use coseismic surface rupture observations by *Quigley et al.* [2012]. These authors documented the Greendale Fault surface rupture during the 2010 Darfield earthquake using GPS surveying, tape measurements, and lidar. They found WNW synthetic Riedel (i.e., synthetic cleavage) dextral shear fractures, NNW antithetic sinistral shear fractures (i.e., antithetic cleavage), NW-SE tension fractures (i.e., extensional fracture), and NE-SW folds and thrust (compressional features compatible with pressure solutions). The consistency of the observed fracture pattern supports the reliability of the proposed fracturing model (see also Table 2).

We perform a second model where we predict the fracture pattern associated only with the regional stress field σ_R . The regional stress orientation (red arrows in Figure 7) is set to be consistent with the fault development and with findings by *Sibson et al.* [2011] and *Holt et al.* [2013]. It is oriented with σ_1 at N115° and σ_3 at N25°, both lying on the horizontal plane, and vertical null σ_2 axis. The regional stress amplitudes are fixed as 30 MPa for σ_1 and −10 MPa for σ_3 , values required to reach the fault failure conditions with the chosen rheological parameters. We use the same σ_R , P_V , and σ_V stress components to calculate σ_A . This second model yields predominant synthetic cleavage striking N85° ± 3.7° and N115° ± 3.7°. Extensional fracture, antithetic cleavage, and pressure solution would develop in N113° ± 3.6°, N145° ± 3.6°, and N23° ± 3.6° directions, respectively (see also Table 3). These directions are consistent with those predicted by *Sibson et al.* [2011], *Townend et al.* [2012], and *Holt et al.* [2013], who all considered an Andersonian wrench regime.

We found that observed polarization better agrees with the first model where fractures are produced by the kinematical-induced elastic stress accumulation on the fault surface. First, fracture orientation is confirmed by the earthquake-induced fracturing at the surface observed after the Darfield 2010 earthquake [*Quigley et al.*, 2012]. Second, the horizontal polarization (N52° ± 27° and N53 ± 23° at stations Dar6 and Dar7, respectively)

shows an overall orthogonal relation with the orientation of the predominant fracture field that is represented in this case by extensional fractures (N139° ± 3.7°) in the kinematic stress model, with a difference of 86°. In the regional stress model, this angle reduces to 60°. The orthogonal relation between ground motion polarization and fractures in fault damage zone has been determined

Table 3. Results From the Regional Stress Model: Fracture Type and Strike

Regional Stress Model	
Fracture	Strike
Extensional fracture (EF)	$113^\circ \pm 3.6^\circ$
Synthetic	$85^\circ \pm 3.7^\circ$
Cleavage (SC)	$115^\circ \pm 3.7^\circ$
Antithetic cleavage (AC)	$145^\circ \pm 3.6^\circ$
Pressure solution (PS)	$23^\circ \pm 3.6^\circ$

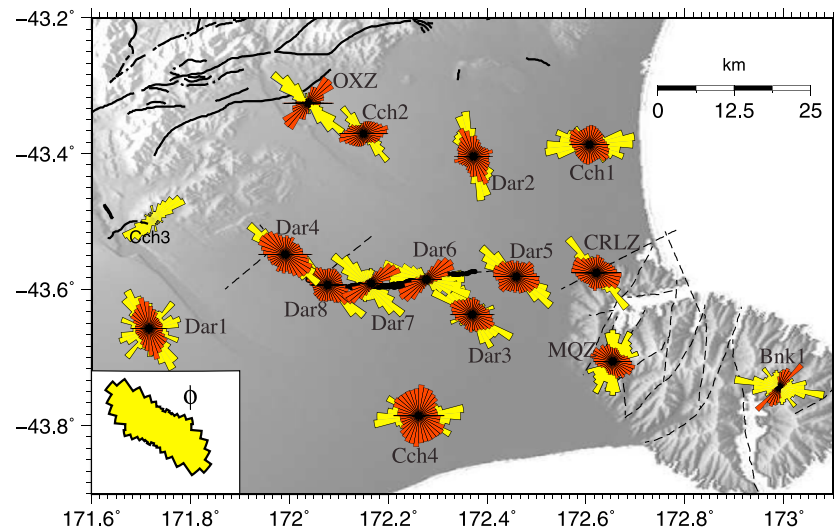


Figure 6. Fast directions from shear wave splitting measurements (yellow rose diagrams) and horizontal ground motion polarization (orange rose diagrams).

in previous studies [Pischiutta *et al.*, 2012, 2013] and was explained as the effect of the higher compliance of fractured rocks in the strike-transverse direction. Moreover, Pischiutta *et al.* [2014] found a recurrent orthogonal relation between horizontal polarization and seismic anisotropy in the Val d'Agri area. They postulated that the existence of an anisotropic medium represented by fractured rocks causes shear wave velocity to be larger in the crack-parallel component (making S wave velocity to be higher in fracture-parallel direction) and compliance to be larger perpendicular to the crack strike (causing ground motion polarization in the fracture-perpendicular direction). To test these findings, we follow Pischiutta *et al.* [2014], and in the next section, we compare ground motion polarization with the seismic anisotropy study by Holt *et al.* [2013].

4.3. Comparison Between Ground Motion Polarization and Seismic Anisotropy

Shear wave splitting was calculated for the stations in this study as well as for a set of short period stations operated by the GeoNet network [Holt *et al.*, 2013]. The general trend of fast orientations of anisotropy in the Canterbury Plains area is nearly parallel to the maximum horizontal stress (S_{Hmax}) of $116 \pm 18^\circ$ determined from focal mechanism inversion. For earthquakes and stations near the middle sector of the fault, both the fast orientation of anisotropy and S_{Hmax} tend to rotate 25° anticlockwise in a more fault-parallel direction.

In order to compare anisotropy and the horizontal polarization we consider fast directions obtained at single stations. In Figure 6 we plot the rose diagrams representing the horizontal polarization (orange) together with rose diagrams of the shear wave splitting fast direction analysis by Holt *et al.* [2013] (yellow). We do not consider stations with scattered rose diagrams of ground motion polarization ($\text{stdev Pol} > 30^\circ$).

On-fault stations Dar 6 and Dar7 and rock-sited stations OXZ in the Canterbury Plains and Bnk1 on Banks Peninsula yield the strongest polarization of ground motion. Those stations also yield strongly aligned fast shear wave splitting.

At Dar7, S wave fast directions follow the general trend, being aligned parallel to S_{Hmax} ($\phi = 138^\circ$) even though the station lies in the fault damage zone. This station shows a nearly orthogonal relation (85°) between the horizontal polarization ($N53^\circ \pm 24^\circ$) and S wave splitting fast direction ($N138^\circ \pm 41^\circ$). At station Dar6, the S wave splitting fast direction is rotated in a counterclockwise direction ($N100^\circ \pm 31^\circ$), tending to be more fault parallel. Holt *et al.* [2013] interpreted the rotation of the fast orientation of anisotropy in terms of stress and fractures in the fault damage zone. These fractures can most likely be represented by the synthetic cleavages ($N101^\circ \pm 3.6^\circ$) produced by the kinematic stress, which are expected to predominate at higher depths (Figure 7b). S wave splitting is controlled by the seismic path and is affected by rock volumes at depths that depend on the hypocentral depth. On the other hand, we consider that ground motion polarization is mainly affected by the uppermost layers, as it is strongly site dependent, independent of earthquake source and path.

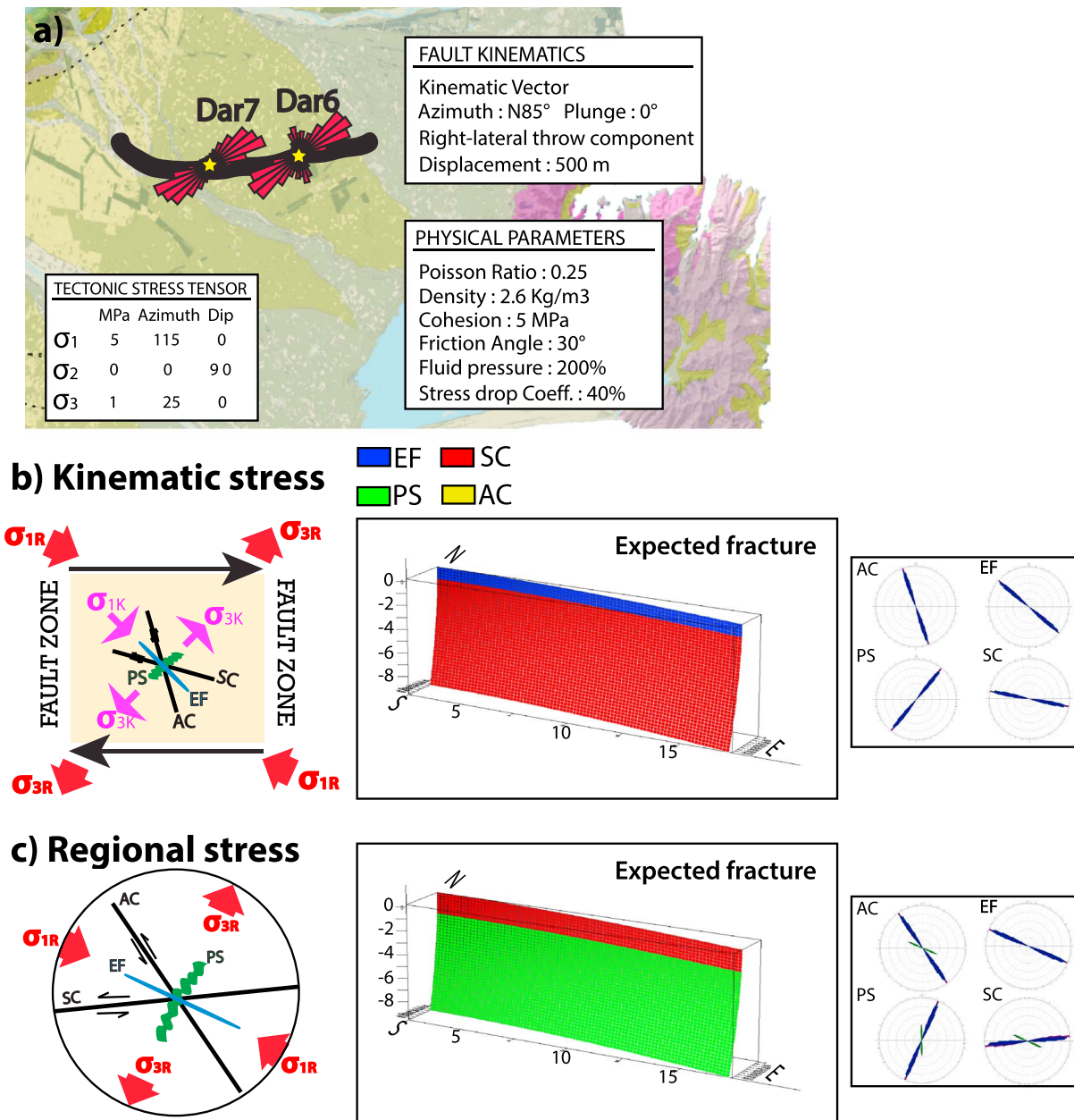


Figure 7. Fracture models of the Greendale Fault yielding the orientation of the expected fracture fields. (a) Map of the Greendale Fault and direction of the observed polarization. The parameters chosen for the model are reported as well. (b) Fault fracture model performed considering the influence of the kinematic stress alone. (c) Fault fracture model considering the influence of the regional stress alone. Red arrows represent the tectonic stress orientation; purple arrows represent the kinematic stress orientation; AC., antithetic cleavage; SC, synthetic cleavage; EF, extensional fracture; PS, pressure solution.

Thus, the nonorthogonal relation between polarization and seismic anisotropy at Dar6 may be related to the different sensitivity at depth of the two methods and to the different fracture distribution (i.e., extensional fractures up to 2 km and synthetic cleavage at higher depths), as determined by the model.

Finally, stations OXZ and Bnk1, located tens of kilometers from the fault also show a nearly orthogonal relation (84° and 78° , respectively) between horizontal polarization ($N44^\circ \pm 27^\circ$ and $N29^\circ \pm 23^\circ$, respectively) and fast direction ($N128^\circ \pm 40^\circ$ and $N107^\circ \pm 50^\circ$). This may indicate that the shear wave splitting and polarization amplification at these two stations are both controlled by the same near-surface fracture distribution.

Conversely to *Pischiutta et al.* [2014], here the comparison between seismic anisotropy and ground motion polarization is more tentative because (i) only two of the four total stations installed in the fault damage

zone (Dar6 and Dar7) show a clear directional amplification effect and (ii) *S* wave fast directions vary between these stations.

5. Concluding Remarks

Polarization analysis performed with both ambient noise and earthquake recordings at stations installed in Canterbury showed an amplitude 4, low-frequency (0.2–0.3 Hz) peak in the ratio of horizontal to vertical components. This is in agreement with results obtained by *Savage et al.* [2013], who applied the cross-correlation technique on the same data set and found a fundamental mode amplification of 4–10 s (0.1–0.25 Hz), which was modeled as surface waves generated in a considerable thickness (1–1.5 km) of unconsolidated sediments over metamorphic bedrock.

Another amplitude peak at higher frequencies (2–5 Hz) was found at two stations installed in the damage zone of the Greendale Fault (Dar6 and Dar7), with amplitudes up to 4. This amplification is strongly anisotropic, with ground motion polarization occurring in the \approx N50° direction. Because this effect is evident only at on-fault stations, it is likely caused by fractured rocks in the fault damage zone, in agreement with previous studies in other regions [*Pischiutta et al.*, 2012, 2013, 2014], which confirms that the process is ubiquitous in fault zones. This directional amplification is not observed on the ambient noise analysis. According to the velocity profile of *Guidotti et al.* [2011], seismic noise in Canterbury is made up of horizontally traveling surface waves with wavelengths of 60–150 m at frequencies of 2–5 Hz. Therefore, directional amplification is not due to shallow heterogeneities throughout the region, but it must be ascribed to fault zone fractured rocks beneath the sediment cover that are sampled by vertically incident body waves of earthquakes and their coda.

In order to interpret results we model the fracture field expected from the Greendale Fault damage zone. We found that fracture orientations produced by kinematic stress accumulation in the fault damage zone agree with the earthquake-induced fracturing at the surface observed after the Darfield 2010 earthquake [*Quigley et al.*, 2012], confirming the reliability of the model. We conclude that the horizontal polarization shows an orthogonal relation with the orientation of the predominant fracture field in the shallow layers (<2 km) of the fault damage zone, which is represented by extensional fractures striking in N139° direction.

Acknowledgments

This study arises from research conducted when M.P. spent 1 month as a visiting scientist at the Victoria University of Wellington, NZ. Data collection for this research was funded by the University of Auckland, the Earthquake Commission (EQC), GNS Science, PASSCAL, and the National Science Foundation (NSF). The data for this paper are available at Victoria University of Wellington data system, the GeoNet system, and the IRIS data center. We thank GeoNet for providing data for their permanent stations. We thank Antonio Rovelli, John Townend, and two anonymous reviewers for comments on earlier versions of the manuscript, and Ellen Syracuse for information on earthquake locations. Maps were made with Generic Mapping Tools (GMT) *Wessel and Smith*, 1998].

References

- Balfour, N. J., M. K. Savage, and J. Townend (2005), Stress and crustal anisotropy in Marlborough, New Zealand: Evidence for low fault strength and structure-controlled, *Geophys. J. Int.*, *163*, 1073–1086, doi:10.1111/j.1365-246X.2005.02783.x.
- Bard, P.-Y. (1998), Microtremor measurements: A tool for site effect estimation, in *Proceeding of the Second International Symposium on the Effects of Surface Geology on Seismic Motion*, edited by K. Irikura et al., pp. 1251–1279, A.A. Balkema, Rotterdam.
- Barnes, P. M. (1995), High-frequency sequences deposited during Quaternary sea-level cycles on a deforming continental shelf, north Canterbury, New Zealand, *Sediment. Geol.*, *97*, 131–156, doi:10.1016/0037-0738(94)00141-G.
- Beavan, J., E. Fielding, M. Motagh, S. Samsonov, and N. Donnelly (2011), Fault location and slip distribution of the 22 February 2011 Mw 6.2 Christchurch, New Zealand, earthquake from geodetic data, *Seismol. Res. Lett.*, *82*(6), 789–799, doi:10.1785/gssrl.82.6.789.
- Beavan, J., M. Mothagh, E. Fielding, N. Donnelly, and D. Collett (2012), Fault slip models of the 2010–2011 Canterbury, New Zealand, earthquakes from geodetic data and observations of postseismic ground deformation, *N. Z. J. Geol. Geophys.*, *55*(3), doi:10.1080/00288306.2012.697472.
- Boness, N., and M. D. Zoback (2004), Stress-induced seismic velocity anisotropy and physical properties in the SAFOD pilot hole in Parkfield, CA, *Geophys. Res. Lett.*, *31*, L15517, doi:10.1029/2003GL019020.
- Boness, N., and M. D. Zoback (2006), Mapping stress and structurally controlled crustal shear velocity anisotropy in California, *Geology*, *34*(10), 825–828, doi:10.1130/G22309.1.
- Browne, G. H., and T. R. Naish (2003), Facies development and sequence architecture of a Late Quaternary fluvial-marine transition, Canterbury Plains and shelf, New Zealand: Implications for forced regressive deposits, *Sediment. Geol.*, *158*, 57–86, doi:10.1016/S0037-0738(02)00258-0.
- Caine, S., J. P. Evans, and C. B. Forster (1996), Fault zone architecture and permeability structure, *Geology*, *24*, 1025–1028, doi:10.1130/0091-7613(1996)024<1025:FZAAPS>2.3.CO;2.
- Cochran, E., Y.-G. Li, and J. E. Vidale (2006), Anisotropy in the shallow crust observed around the San Andreas Fault before and after the 2004 M 6.0 Parkfield earthquake, *Bull. Seismol. Soc. Am.*, *96*(4B), S364–S375, doi:10.1785/0120050804.
- Cochran, E. S., J. E. Vidale, and Y.-G. Li (2003), Near-fault anisotropy following the Hector Mine earthquake, *J. Geophys. Res.*, *108*(B9), 2436, doi:10.1029/2002JB002352.
- Crampin, S. (1994), The fracture criticality of crustal rocks, *Geophys. J. Int.*, *118*(2), 428–438, doi:10.1111/j.1365-246X.1994.tb03974.x.
- Crampin, S., and D. C. Booth (1985), Shear-wave polarization near the North Anatolian fault—II. Interpretation in terms of crack-induced anisotropy, *Geophys. J. R. Astron. Soc.*, *83*, 75–92.
- Cubrinovsky, M., J. D. Bray, M. Taylor, S. Giorgini, B. Bradley, L. Wotherspoon, and J. Zupan (2011), Soil liquefaction effects in the central business district during the February 2011 Christchurch earthquake, *Seismol. Res. Lett.*, *82*, 893–904, doi:10.1785/gssrl.82.6.893.
- Di Giulio, G., F. Cara, A. Rovelli, G. Lombardo, and R. Rigano (2009), Evidences for strong directional resonances in intensely deformed zones of the Pernicana fault, Mount Etna, Italy, *J. Geophys. Res.*, *114*, B10308, doi:10.1029/2009JB006393.

- Di Giulio, G., A. Rovelli, F. Cara, P. P. Bruno, M. Punzo, and F. Varriale (2013), A controlled-source experiment to investigate the origin of wavefield polarization in fault zones, paper presented at IAHS-IAPSO-IASPEI Joint Assembly, 22–26 July 2013, Gothenburg, Sweden (abstract n. 2843253).
- do Nascimento, A., R. Pearce, and M. Takeya (2002), Local shear-wave observations in Joao Camara, NE Brazil, *J. Geophys. Res.*, *107*(B10), 2232, doi:10.1029/2001JB000560.
- Falsaperla, S., F. Cara, A. Rovelli, M. Neri, B. Behncke, and V. Acocella (2010), Effects of the 1989 fracture system in the dynamics of the upper SE flank of Etna revealed by volcanic tremor data: The missing link?, *J. Geophys. Res.*, *115*, B11306, doi:10.1029/2010JB007529.
- Forsyth, P. J., D. J. A. Barrell, and R. Jongens (2008), Geology of the Christchurch area: Institute of Geological and Nuclear Sciences Geological Map 16 scale 1:250,000, 1 sheet, 67 p. text.
- Ghisetti, F. C., and R. H. Sibson (2012), Compressional reactivation of E–W inherited normal faults in the area of the 2010–2011 Canterbury earthquake sequence, *N. Z. J. Geol. Geophys.*, *55*(3), 177–184, doi:10.1080/00288306.2012.674048.
- Gledhill, K., J. Ristau, M. Reyners, B. Fry, and C. Holden (2011), The Darfield (Canterbury, New Zealand) Mw 7.1 earthquake of September 2010: A preliminary seismological report, *Seismol. Res. Lett.*, *82*, 379–386, doi:10.1785/gssrl.82.3.378.
- Guidotti, R., M. Stupazzini, C. Smerzini, R. Paolucci, and P. Ramieri (2011), Numerical study on the role of basin geometry and kinematic seismic source in 3D ground motion simulation of the 22 February 2011 Mw 6.2 Christchurch earthquake, *Seismol. Res. Lett.*, *82*, 767–782, doi:10.1785/gssrl.82.6.767.
- Hampton, S. J., and J. W. Cole (2008), Lyttelton Volcano, Banks Peninsula, New Zealand: Primary volcanic landforms and eruptive centre identification, *Geomorphology*, *104*, 284–298, doi:10.1016/j.geomorph.2008.09.005.
- Hanks, T. C., and W. H. Bakun (2002), A bilinear source-scaling model for M–log A observations of continental earthquakes, *Bull. Seismol. Soc. Am.*, *92*, 1841–1846, doi:10.1785/0120010148.
- Hanks, T. C., and W. H. Bakun (2008), M–log A observations for recent large earthquakes, *Bull. Seismol. Soc. Am.*, *98*, 490–494, doi:10.1785/0120070174.
- Harding, T. P. (1974), Petroleum traps associated with wrench faults, *Bull. Am. Assoc. Petrol. Geol.*, *60*, 365–378.
- Harding, T. P., and J. D. Lowell (1979), Structural styles, their plate tectonic habitats and hydrocarbon traps in petroleum provinces, *Bull. Am. Assoc. Petrol. Geol.*, *63*, 1016–1058.
- Herzer, R. H. (1979), *Banks Sediments. Coastal Chart Series 1:200 000 Sediments*, New Zealand Oceanographic Institute, Dep. of Scientific and Industrial Research, Wellington, New Zealand.
- Hobbs, B. E., W. D. Means, and P. P. Williams (1976), *An Outline of Structural Geology*, 571 pp., Wiley, New York.
- Holden, C. (2011), Kinematic source model of the 22 February 2011 Mw 6.2 Christchurch earthquake using strong motion data, *Seismol. Res. Lett.*, *82*, 783–788, doi:10.1785/gssrl.82.6.783.
- Holt, R. A., M. K. Savage, J. Townend, E. M. Syracuse, and C. H. Thurber (2013), Crustal stress and fault strength in the Canterbury Plains, New Zealand, *Earth Planet. Sci. Lett.*, *383*(173–181), 2013, doi:10.1016/j.epsl.2013.09.041.
- Jongens, R., D. Barrell, J. K. Campbell, and J. R. Pettinga (2012), Faulting and folding beneath the Canterbury Plains identified prior to the 2010 emergence of the Greendale Fault, *N. Z. J. Geol. Geophys.*, *55*, doi:10.1080/00288306.2012.674050.
- Jurkevics, A. (1988), Polarization analysis of three component array data, *Bull. Seismol. Soc. Am.*, *78*, 1725–1743.
- Kaiser, A., et al. (2012), The Mw 6.2 Christchurch earthquake of February 2011: Preliminary report, *N. Z. J. Geol. Geophys.*, *55*(1), 67–90, doi:10.1080/00288306.2011.641182.
- Kanasewich, E. R. (1981), *Time Sequence Analysis in Geophysics*, 477 pp., Univ. of Alberta press, Edmonton.
- Kane, D. L., P. M. Shearer, B. P. Goertzel-Allmann, and F. L. Vernon (2013), Rupture directivity of small earthquakes at Parkfield, *J. Geophys. Res. Solid Earth*, *118*, 212–221, doi:10.1029/2012JB009675.
- Laird, M. G., and J. D. Bradshaw (2004), The break-up of a long-term relationship: The Cretaceous separation of New-Zealand from Gondwana, *Gondwana Res.*, *7*(1), 273–286, doi:10.1016/S1342-937X(05)70325-7.
- Li, Y.-G., G. P. De Pascale, M. C. Quigley, and D. M. Gravley (2014), Fault damage zones of the M7.1 Darfield and M6.3 Christchurch earthquakes characterized by fault-zone trapped waves, *Tectonophysics*, *618*, 79–101, doi:10.1016/j.tecto.2014.01.029.
- Liu, Y., S. Crampin, and I. Main (1997), Shear-wave anisotropy: Spatial and temporal variations in time delays at Parkfield, Central California, *Geophys. J. Int.*, *130*, 771–785, doi:10.1111/j.1365-246X.1997.tb01872.x.
- Mackinnon, T. C. (1983), Origin of the Torlesse terrane and coeval rocks, South Island, New Zealand, *Geol. Soc. Am. Bull.*, *94*, 967–985, doi:10.1130/0016-7606(1983)94<967:OOTTA>2.0.CO;2.
- Mandl, G. (2000), *Faulting in Brittle Rocks*, 434 pp., Springer, London.
- Moar, N. T., and M. Gage (1973), Interglacial deposits in Joyces Stream (S74), Waimakariri valley, Canterbury, *N. Z. J. Geol. Geophys.*, *16*, 321–331, doi:10.1080/00288306.1973.10431361.
- Nur, A., and G. Simmons (1969), Stress-induced velocity anisotropy in rock: An experimental study, *J. Geophys. Res.*, *74*(27), 6667–6674, doi:10.1029/JB074i027p06667.
- Orense, R. P., T. Kiyota, S. Yamada, M. Cubrinovski, Y. Hosono, M. Okamura, and S. Yasuda (2011), Comparison of liquefaction features observed during the 2010 and 2011 Canterbury earthquakes, *Seismol. Res. Lett.*, *82*, 905–926, doi:10.1785/gssrl.82.6.905.
- Panzer, F., M. Pischiutta, G. Lombardo, C. Monaco, and A. Rovelli (2014), Wavefield polarization in fault zones of the western flank of Mt. Etna: Observations and fracture orientation modelling, *Pageoph*, doi:10.1007/s00024-014-0831-x.
- Paulsen, H. (2004), Crustal anisotropy in southern California from local earthquake data, *Geophys. Res. Lett.*, *31*, L01601, doi:10.1029/2003GL018654.
- Peng, Z., and Y. Ben-Zion (2004), Systematic analysis of crustal anisotropy along the Karadere-Duzce branch of the North Anatolian Fault, *Geophys. J. Int.*, *159*, 253–274, doi:10.1111/j.1365-246X.2004.02379.x.
- Pischiutta, M., F. Salvini, J. Fletcher, A. Rovelli, and Y. Ben-Zion (2012), Horizontal polarization of ground motion in the Hayward fault zone at Fremont, California: Dominant fault-high-angle polarization and fault-induced cracks, *Geophys. J. Int.*, *188*(3), 1255–1272, doi:10.1111/j.1365-246X.2011.05319.x.
- Pischiutta, M., A. Rovelli, F. Salvini, G. Di Giulio, and Y. Ben-Zion (2013), Directional resonance variations across the Pernicana fault, Mt. Etna, in relation to brittle deformation fields, *Geophys. J. Int.*, *193*, 986–996, doi:10.1093/gji/ggt03.
- Pischiutta, M., M. Pastori, L. Impropa, F. Salvini, and A. Rovelli (2014), Orthogonal relation between wavefield polarization and fast S-wave direction in the Val d'Agri region: An integrating method to investigate rock anisotropy, *J. Geophys. Res. Solid Earth*, *119*, 1–13, doi:10.1002/2013JB010077.
- Quigley, M., et al. (2010), Surface rupture of the Greendale Fault during the Mw 7.1 Darfield (Canterbury) earthquake, New Zealand: Initial findings, *Bull. New Zeal. Soc. Earthquake Eng.*, *43*(4), 236–242, doi:10.1130/G32528.1.
- Quigley, M., R. Van Dissen, N. Litchfield, P. Villamor, B. Duffy, D. Barrell, K. Furlong, T. Stahl, E. Bilderback, and D. Noble (2012), Surface rupture during the 2010 Mw 7.1 Darfield (Canterbury) earthquake: Implications for fault rupture dynamics and seismic-hazard analysis, *Geology*, *40*, 55–58, doi:10.1130/G32528.1.

- Riedel, W. (1929), Zur mechanik geologischer Brucherscheinungen, *Zentralblatt. Miner. Geol. Palaont. B*, 354–368.
- Salvini, F., A. Billi, and D. U. Wise (1999), Strike-slip fault-propagation cleavage in carbonate rocks: The Mattinata Fault Zone, Southern Apennines, Italy, *J. Struct. Geol.*, 21, 1731–1749, doi:10.1016/S0191-8141(99)00120-0.
- Savage, M., F.-C. Lin, and J. Townend (2013), Ambient noise cross-correlation observations of fundamental and higher-mode Rayleigh wave propagation governed by basement resonance, *Geophys. Res. Lett.*, 40, 3556–3561, doi:10.1002/grl.50678.
- Sewell, R. J. (1988), Late Miocene volcanic stratigraphy of central Banks Peninsula, Canterbury, New Zealand, *N. Z. J. Geol. Geophys.*, 31, 41–64, doi:10.1080/00288306.1988.10417809.
- Sibson, R., F. Ghisetti, and J. Ristau (2011), Stress control of an evolving strike-slip fault system during the 2010–2011 Canterbury, New Zealand, earthquake sequence, *Seismol. Res. Lett.*, 82, 824–832, doi:10.1785/gssrl.82.6.824.
- Spudich, P., M. Hellweg, and H. K. Lee (1996), Directional topographic site response at Tarzana observed in aftershocks of the 1994 Northridge California earthquake: Implications for mainshock motions, *Bull. Seismol. Soc. Am.*, 86, 193–208.
- Syracuse, E. M., R. A. Holt, M. K. Savage, J. H. Johnson, C. H. Thurber, K. Unglert, K. N. Allan, S. Karalliyadda, and M. Henderson (2012), Temporal and spatial evolution of hypocentres and anisotropy from the Darfield aftershock sequence: Implications for fault geometry and age, *N.Z. J. Geol. Geophys.*, 55(3), 287–293, doi:10.1080/00288306.2012.690766.
- Syracuse, E. M., C. H. Thurber, C. J. Rawles, M. K. Savage, and S. Bannister (2013), High-resolution relocation of aftershocks of the Mw 7.1 Darfield, New Zealand, earthquake and implications for fault activity, *J. Geophys. Res. Solid Earth*, 118, 4184–4195, doi:10.1002/jgrb.50301.
- Townend, J., S. Sherburn, R. Arnold, C. Boese, and L. Woods (2012), Three-dimensional variations in present-day tectonic stress along the Australia–Pacific plate boundary in New Zealand, *Earth Planet. Sci. Lett.*, 353–354, 47–59, doi:10.1016/j.epsl.2012.08.003.
- Turcotte, D., and G. Schubert (1982), *Geodynamics; Applications of Continuum Physics to Geological Problems*, 450 pp., John Wiley, New York.
- Van Dissen, R., et al. (2011), Surface rupture displacement on the Greendale Fault during the Mw 7.1 Darfield (Canterbury) earthquake, New Zealand, and its impact on man-made structures, *Proc. Ninth Pac. Conf. Earthquake Eng.*, pp. 186–193, Building an Earthquake-Resilient Society, Auckland, New Zealand, 14–16 April.
- Walsh, J. J., and J. Watterson (1988), Analysis of the relationship between displacements and dimensions of faults, *J. Struct. Geol.*, 10(3), 239–247, doi:10.1016/0191-8141(88)90057-0.
- Wessel, P., and W. H. F. Smith (1998), New, improved version of Generic Mapping Tools released, *Eos Trans. AGU*, 79(47), 579.
- Zhang, Z., and S. Y. Schwartz (1994), Seismic anisotropy in the shallow crust of the Loma Prieta segment of the San Andreas Fault System, *J. Geophys. Res.*, 99(B5), 9651–9661, doi:10.1029/94JB00241.
- Zinke, J. C., and M. D. Zoback (2000), Structure-related and stress-induced shear-wave velocity anisotropy: Observations from microearthquakes near the Calaveras fault in central California, *Bull. Seismol. Soc. Am.*, 90(5), 1305–1312, doi:10.1785/0119990099.